LAWRENCE
LIVERMORE
NATIONAL
LABORATORY

LLNL-TR-681009

Technical Reports - FY16 Q1 - October-December 2015

V. Lordi, B. M. Rubenstein, K. G. Ray

January 20, 2016

Disclaimer

This work performed under the auspices of the U.S. Department of Energy by Lawrence Livermore National Laboratory under Contract DE-AC52-07NA27344.

Technical Reports – FY16 Q1 – October-December 2015

Project: LEUCITE BOUNTY
PI: Vincenzo Lordi, lordi2@llnl.gov, 925-423-2755
Location: Lawrence Livermore National Laboratory

Programmatic POC: Chris Johnson, 301-226-8911
Technical POC: Chris Richardson, 301-935-6426

Date: January 15, 2016

Attached are two technical reports summarizing progress during the October-December 2015 quarter on each of the two project tasks:

- "Microscopic Models of Anomalous Heating in Ion Traps"
- "Epitaxial Aluminum Collaboration"

This work was performed under the auspices of the U.S. Department of Energy by Lawrence Livermore National Laboratory under Contract DE-AC52-07NA27344. LLNL-TR-681009

Quarterly Report (Sept-Dec, 2015): Microscopic Models of Anomalous Heating in Ion Traps

Brenda Rubenstein, Keith Ray, and Vincenzo Lordi
Lawrence Livermore National Laboratory
January 15, 2016

I. OVERVIEW OF RECENT PROGRESS

Recent experiments have demonstrated that the frequency dependence of motional heating rates in ion traps can vary dramatically with temperature.[1-6] More specifically, it has been shown that, at temperatures below roughly 70 K, heating rates are substantially lower than those observed at temperatures above 70 K.[1,2] These observations, combined with experiments that show that ion bombardment may also reduce heating rates,[4,5] suggest that one potential source of heating may be the presence of unwanted adatoms on trap surfaces. Based upon this evidence, this past quarter, we have used our previously detailed microscopic model of anomalous heating to study which adatoms may be responsible for the observed temperature-dependent scaling of motional heating rates with frequency. We have also examined the validity of one of the key assumptions in our model - that surface adatom dipoles can be accurately obtained from a variational ansatz - by using more direct DFT calculations of the dipole moments. Our current results suggest that the adatoms potentially responsible for the observed motional heating rates should bind weakly to the electrode surface and likely have a mass that exceeds that of Ne. Preliminary DFT calculations suggest that an analytical adatom dipole model,[9] previously used in the ion trap noise literature[7] to obtain the dipole as a function of adatom-surface distance, may be insufficiently accurate. Therefore, we are working toward obtaining a tabulation of the distance-dependent dipole for several adsorbates using first principles calculations for more accurate input to the heating model. The accurate calculation of the adatom dipole is important because its fluctuation is what couples to and heats the trapped ion qubit. Future work will focus on calculating the frequency spectra of a variety of hydrocarbons, which should have the binding characteristics identified below as necessary for reproducing experimental results. Upcoming efforts will moreover be directed toward deriving an improved microscopic model of heating which will enable direct comparisons of heating rates with measured ion-surface distances and will more accurately account for experimental parameters such as the trapping frequency, ion-electrode distance, and RF power applied to the electrodes.

II. TEMPERATURE DEPENDENCE OF THE FREQUENCY SCALING FOR A VARIETY OF ADATOMS

In order to refine our understanding of which adatoms may be responsible for surface heating (as well as to validate our microscopic model), we used highly accurate dispersion-corrected DFT calculations to compute the adatom-electrode interaction potentials of a variety of simple adatoms, including Ne, H, O, S, and C, on a gold surface. These potentials were first computed at roughly 20 values of the adatom-surface vertical distance for each of the adatom-electrode combinations using the PBE, LDA, vdW-DF, vdW-DF2, and vdW-DF-optB88 functionals. Final potential values were subsequently refined using the more computationally expensive vdW-DF-cx functional. As described in our previous quarterly report, we then fit these potential points to continuous functions (see Appendix, Figures A1-A6 and Table A1) and computed their related dipole moments, dipole-dipole correlation functions, and spectra at a variety of temperatures.

The behavior of the correlation functions and spectra obtained for all of the adatom-electrode combinations largely boiled down to the value of the parameter $T^*=E_{10}/(k_BT)$, where E_{10} denotes the energy difference between the ground and first excited vibrational states of the adatom-electrode potential, k_B is Boltzmann's constant, and T is the temperature of the system in Kelvin. As expected, when $T^*>1$, the systems largely exhibited two-state behavior in which only the first two vibrational states of the potential were populated because thermal fluctuations were insufficient for surmounting the E_{10} energy barrier. For $T^*<1$, however, the systems occupied multiple vibrational states. Indeed, for

T*<0.167, all vibrational states were nearly equally occupied (not shown below). This trend is illustrated in Figures 1 and 2 for the Ne-Au adatom-electrode combination. Until a temperature of roughly T*=1, the population of the second excited state is less than 5% of the total population. It is only below this T* that the second excited state is populated above the 10% level.

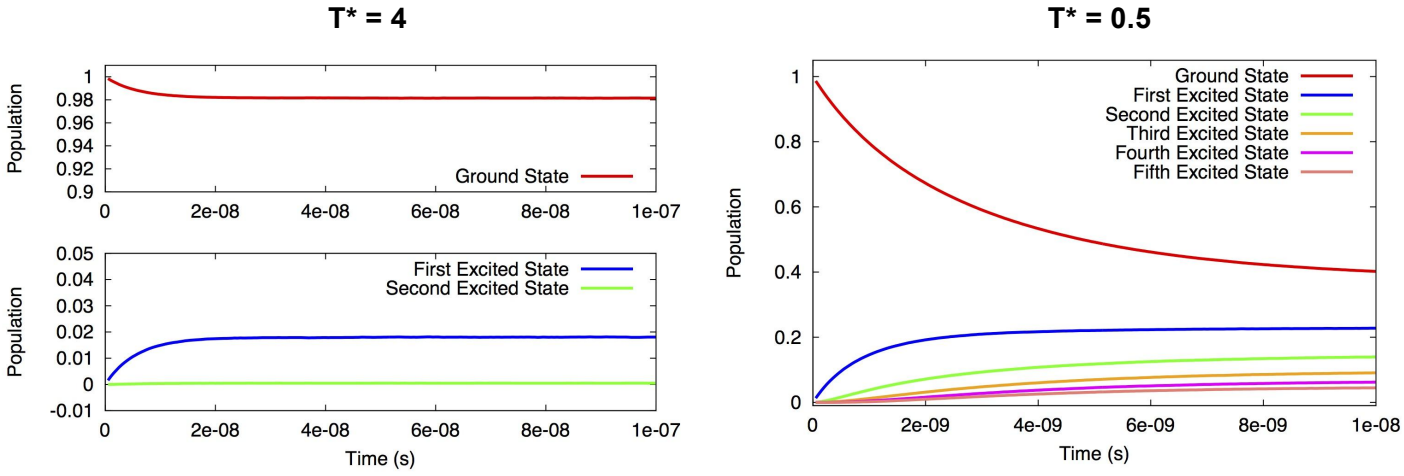

Figure 1:
The populations of the ground and excited vibrational states of the Ne-Au potential. **Left: T*=4 (4.49 K); Right: T*=0.5 (35.93 K).** As seen in the figure on the left, at low temperatures, only the first two vibrational states are occupied to any significant degree. As expected, as the temperature is increased, more states are populated as seen in the figure on the right, ushering in the transition to multi-state behavior. We observe similar trends for all of the adatom-electrode potentials studied.

Figure 2:
The population of the third vibrational state (second excited state) of the Ne-Au adatom-electrode interaction potential at a variety of temperatures. It is only below T*=1 that the third vibrational state begins to be appreciably occupied.

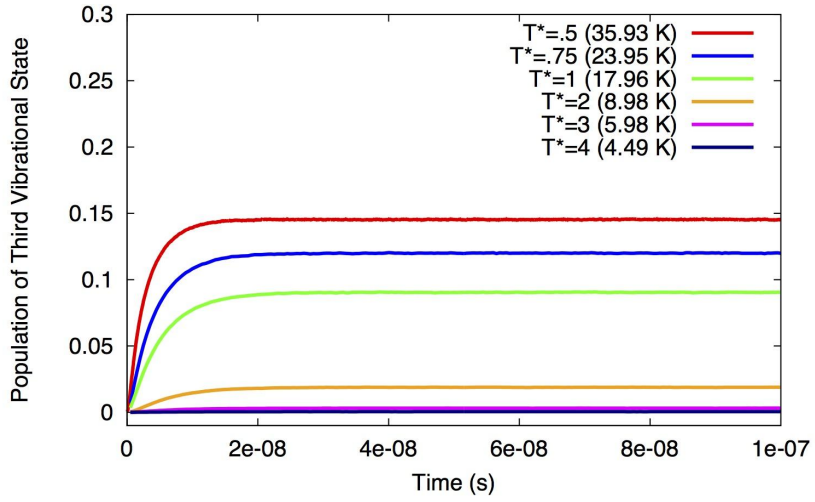

The transition to multi-state behavior at lower T* very clearly manifests itself in the related dipole-dipole correlation functions. As shown below in Figure 3 for H-Au and Figure 4 for Ne-Au, the dipole-dipole correlation functions decay at roughly the same rate for all values of T* below 1 (for the exact decay constants, see Tables 1 and 2).

Below T*=1, the correlation functions decay several times faster than above this reduced temperature. Consequently, it is at T*=1 that changes in the frequency-dependent scaling of dipole-dipole spectra are expected.

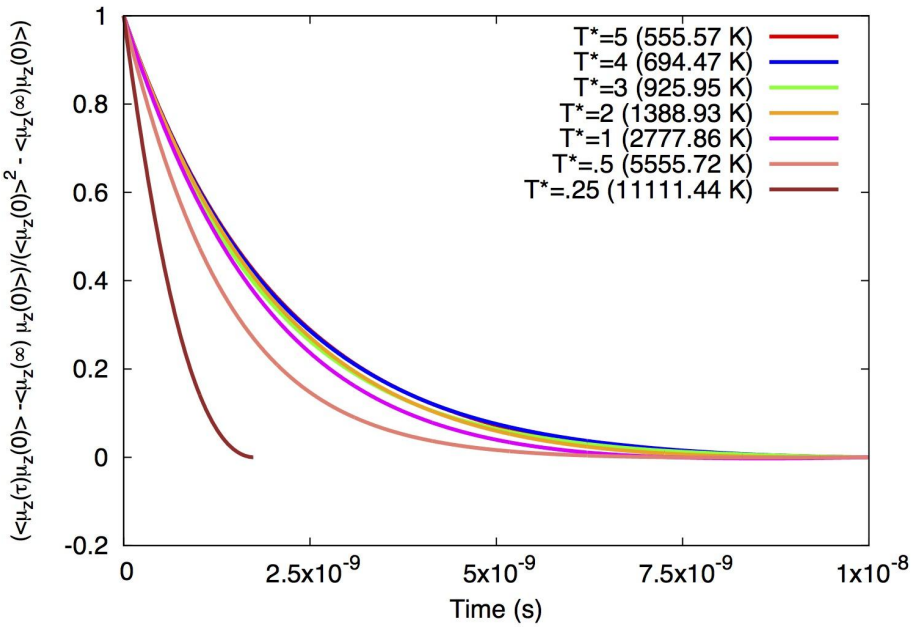

Figure 3:
The normalized dipole-dipole correlation functions for the H-Au potential at a variety of temperatures. The decay rates of the correlation functions are roughly the same for T*>1. Below T*=1, the correlation functions decay significantly faster than for values of T* above 1.

Figure 4:
The same as Figure 3, but for the Ne-Au adatom-electrode combination. A similar trend, in which the decay rates increase dramatically below T*=1, is seen in all of the adatom-electrode surface combinations studied here.

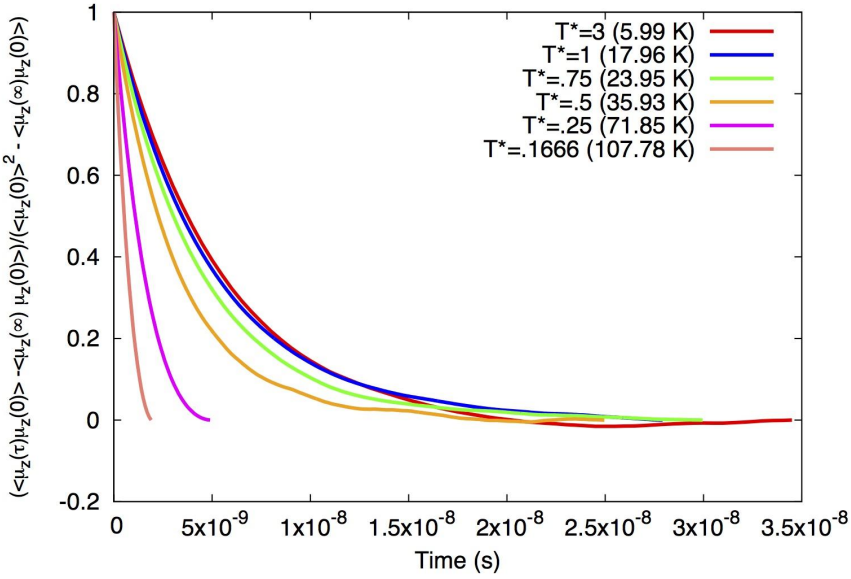

H–Au Interaction Potential	
T*	**Decay Constant (Hz)**
4	5.05×10^8
3	5.37×10^8
2	5.64x108
1	5.80×10^8
0.5	7.53×10^8
0.25	1.72×10^9

Table 1
The dipole-dipole correlation function decay constants for the H-Au interaction potential at a variety of temperatures. Again, a large increase in these decay constants is observed for T*<1.

Ne-Au Interaction Potential	
T*	**Decay Constant (Hz)**
4.5	2.03×10^8
4	1.87×10^8
3	1.93×10^8
2	1.86x108
1	1.97×10^8
0.75	2.28×10^8

Table 2
The same as in Table 1, but for the Ne-Au system.

While we only present results here for the H-Au and Ne-Au systems for the sake of space, similar features were observed in all of the adatom-electrode combinations simulated. What differs among the systems is the physical temperature to which T* corresponds. The physical meaning of T* depends on the value of E_{10}, which in turn depends on the adatom mass and the adatom-electrode potential well-depth. For strongly bound, light adatoms like hydrogen, T*=1 corresponds to a relatively high temperature, often several times room temperature; for weakly bound, heavy adatoms like Ne, T*=1 corresponds to a physical temperature of tens of K. Thus, the temperature where multistate behavior is expected to manifest itself in the computed spectra is dependent upon the difference between the ground and first excited state vibrational energies. Table 3 gives a rough estimation of the maximum E_{10} values necessary to observe spectral changes at a given temperature, assuming that spectral changes manifest at T*<1. For example, in order to see a change in the frequency dependence of the spectra at T=50K, the energy difference required would be $E_{10} < 0.158$ mHa.

Temperature (K)	Maximum E_{10} Required to See a Transition at the Given Temperature (mHa)
10	0.0317
20	0.0633
30	0.0950
40	0.127
50	0.158
60	0.190
70	0.222
80	0.253
90	0.285
100	0.317
150	0.475
200	0.633
250	0.792
300	0.050
350	1.11
400	1.27
450	1.423
500	1.58
550	1.74
600	1.90

Table 3

The approximate differences between the ground and first excited state energies, E_{10}, needed to observe changes in the scaling of the frequency spectra at the given temperatures. Note that experiments see a change in the frequency dependent scaling at several tens of K, which would correspond to energy differences less than about 0.25 mHa.

The values in Table 3 may be used to predict which adatom-electrode combinations will manifest spectral changes in the temperature regimes seen in experiments. As discussed in References 1 and 2, experimental spectra undergo a change in their frequency-dependent scaling around 50-70 K. As shown in Table 4, the only adatom-electrode combination studied above with an energy difference sufficiently small to manifest spectral changes at 50 K are Ne-Au, Ne-Ag, or He-Au, with He having an E_{10} very close to the cross-over. Thus, Ne is the best candidate. However, Ne is rarely present in experiments and so is unlikely to be the adatom responsible for the observed spectral changes. Much more likely culprits on Au are molecules similar or more weakly binding as Ne and similar or more massive than Ne. Such molecules probably include a variety of hydrocarbons and hydrocarbon fragments. The potentials and related spectra of several hydrocarbons, such as benzene and methane, are currently being computed to further explore this idea and will be reported in the future. Upcoming results on these spectra will not only test the predictive power of our model, but also can help physicists hone down the types of species that may be causing anomalous motional heating in their traps.

Adatom-Electrode Combination	Energy Difference Between Ground and 1st Excited State (mH)
Ne-Au	0.0633
H-Au	8.80
S-Au	1.70
He-Au	0.160
C-Au	2.01
Ne-Ag	0.0903

Table 4

The energy difference between the ground and first excited states, E_{10}, for the electrode-substrate combinations thus far explored in this work. He-Au, Ne-Au, and Ne-Ag are sufficiently weakly bound and heavy to be candidates for inducing frequency-dependent changes around 50-70K ($E_{10} \sim 0.158$-0.222 mHa; see Table 3). This suggests that even heavier, less bound adatoms/admolecules may be responsible for motional heating in the regimes seen in experiments.

III. ADATOM-ELECTRODE DIPOLE MOMENTS

To accurately model the dipole fluctuations of adsorbed species on trap electrodes, we first must have an accurate model of the dipole of the adsorbate as a function of distance from the electrode.

A previously used variational model[9] in the ion trap literature[7] is given by

$$P = \langle \varphi | \sum_i e z_i | \varphi \rangle$$
$$= \frac{3e^2 m}{4\hbar^2 R_0^4} \sum_i (z_i^2)_{00} \left[(z_i^4)_{00} + \tfrac{1}{2} (z_i^2 \rho_i^2) \right]_{00},$$

where P is the dipole moment of the adatom, m is the mass of the electron, R_0 is the distance from the substrate, $(\text{Obs.})_{00}$ is the expectation value of the observable, Obs., in the ground state 0, z_i is the distance of the electron from the nucleus in the direction normal to the substrate, ρ_i is the distance of the electron from the nucleus parallel to the substrate, and the sum is over all electrons in the adatom. For hydrogen, this reduces to the expression

$$P = 0.47 e a_0^{1/2} \alpha^{3/2} / R_0^4.$$

where a_0 is the bohr radius, α is the polarizability of hydrogen, and R_0 is the distance from the adatom to the substrate. This model produces a dipole vs. distance curve as depicted in Figure 5. This model is based on the interaction of the adatom with its image charge in the metal (see Figure 6a). Further from the electrode, the induced adatom dipole due to this effect diminishes as $1/R_0^4$, and an interaction with the electrode surface dipole will dominate, which creates a dipole of opposite direction on the adatom. These two effects are illustrated in Figure 6.

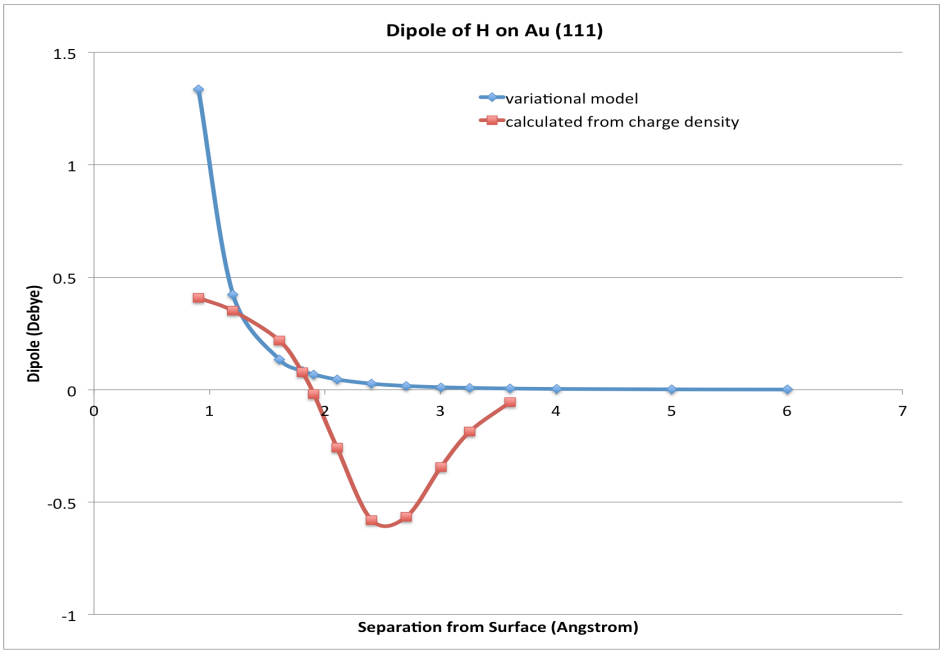

Figure 5:
The dipole moment of H on Au(111) as a function of distance calculated using either the DFT charge density (red) or a variational model based only on image charges (blue).[9] The equilibrium separation for the bound H from the surface is 1.6 Å.

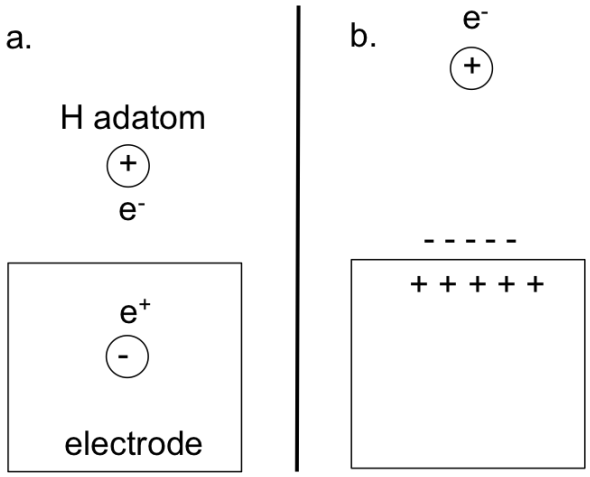

Figure 6:
The induced dipole on an H adatom, with a nucleus and single electron, is schematically shown for (a) the short-distance case and (b) long-distance case. In (a), the image charge in the metal electrode induces the dipole on the H atom, and in (b), the surface dipole of the metal induces the dipole on the H atom.

In order to validate the variational model given above, we calculated the dipole using first principles calculations. As with the binding potential curves, we utilized the vdW-DF-cx functional within density functional theory. We integrate the charge density over the cell to obtain the adatom dipole moment, and repeat the procedure for several adatom-surface separations. The results for H-Au are given in Figure 5, compared to the model described above. Since the variational model does not capture the interaction with the intrinsic metal surface dipole, as depicted in Figure 6b, the dipole vs. distance results from DFT do not qualitatively match those given by the variational model for separations larger than ~2 Å. The very short distance dipole is also over-estimated by the variational model. The impact on computed noise spectra will vary in each specific case and depend on the maximum excursion during adatom vibrations.

Going forward, we will calculate and tabulate the distance-dependent dipole for each adsorbate we consider using density functional theory. In addition, during the course of these preliminary calculations, we identified a computational detail that can affect the accuracy of the dipole moment calculated in periodic density functional theory, which is the potential created by the periodic images of the dipole across the computational supercell boundaries. This error can be corrected quite accurately even for modest slab-slab vacuum separations by applying an electrostatic potential correction within the DFT calculation. The results shown in Figure 5 did not include this correction and will change slightly once the corrected calculations are completed, however the qualitative shape, which differs from the variational model, should remain the same.

IV. CHALLENGES AND FUTURE WORK

In Sections II and III, we have outlined our most recent work studying the effects of a variety of adatom-electrode combinations and a more accurate treatment of dipole moments on spectral changes. Our results thus far are promising in the sense that, given a fairly simple model, they seem capable of predicting which adatoms may be responsible for heating in different temperature and frequency regimes. Direct extensions of this quarter's work will entail further varying the electrode materials and adsorbates used in our calculations and developing a way to properly model the internal vibrational degrees of freedom present in molecular adsorbates (*e.g.*, hydrocarbons and their fragments). First principles calculations will be used to calculate the dipole moments of these additional systems.

Looking even further forward, we would like to challenge and adapt our microscopic model by directly comparing its spectral results to those produced in a variety of experimental situations. Specifically, we would like to ascertain the exact scaling of our spectra and compare the exponents we find with those previously published.[1-6] Further, longer term adjustments and extensions of our model must additionally be made to capture:

- **2D adatom-electrode potentials**, which will more accurately represent the change in potentials observed as an adatom moves across different parts of the electrode surface.
- **The heating rates at different trapped ion distances above the surface**. Currently, our model does not predictively account for the changes induced by bringing the ion closer to or further from the electrode surface, since that distance enters the model only through scaling, which has an assumed distance dependence.
- **Electrode surface roughness**. Recent experimental work suggests that heating may also be related to changes in the texture of the surface at different temperatures and before/after ion bombardment.[8] We would like to characterize the effects that surface texture brings about.
- **Possible changes in the adatom binding and vibrations due to the applied RF and/or static electric potential on the electrode.** Changing the potential on the electrode changes the Fermi level and may strengthen or weaken the binding of adatoms. This, in turn, would change their vibrational frequencies/dipole fluctuations and, consequently, the noise affecting the trapped ion.

The greatest challenge to our future progress will be re-deriving a model that accounts for all of these features from first principles, in particular accounting more directly for coupling mechanisms to the trapped ion's motion, which may involve the applied RF and/or static potentials on the electrodes in a coupled way. Work has already begun on this and the other fruitful directions listed above, which we hope to discuss in greater detail next quarter.

V. APPENDIX: FITS TO THE ADATOM-ELECTRODE INTERACTION POTENTIALS

As discussed in Section II, before correlation functions and spectra could be calculated, fits had to be made to the adatom-electrode interaction potentials. These potentials were first obtained at around 20 points using DFT and the fits connected these points into smooth, integrable curves. In most cases in which the adatom was strongly repelled by the surface (Ne-Au, H-Au, S-Au, Ne-Ag), the potentials could be fit by the standard Exp-3 potential with some additional dispersion terms to better capture the long-range behavior. However, in a few cases in which the adatom was not repelled by the surface at small distances (C-Au and O-Au), alternative or harmonic fits had to be performed, to at least capture the behavior of the potential around its minimum. All of these fits are illustrated in Figures A1-A6. The related potentials are given in Table A1.

Adatom-Electrode Interaction	Best Fit Interaction Potential, $V(z)$ (Ha)
Ne-Au	$0.000478*e^{5.765(1-z/5.86011)}-0.184998z^{-3}$
H-Au	$-.44578e^{3.534*(1-z/3.0227)}+-.8287z^{-3}+735.368z^{-6}-5705.91z^{-8}+18440.4z^{-10}+-22493.3z^{-12}$
O-Au	$.070248-.217992z+.0806829z^{2}-.0104304z^{3}+.000446365z^{4}-.00110197z^{-2}$
S-Au	$.312049-.566275z+.014464z^{2}+.109833z^{-2}+6.20855^{-.822971z}+2.75919\log(.410941z)$
C-Au	$-.160937+.0419065(z-2.24414589)^{2}$
Ne-Ag	$57.238e^{3.8305*(1-z/2.9278)}-1834.64z^{-3}$

Table A1

Best fits to a variety of adatom-electrode interactions as calculated using DFT. These fits were used to compute the dipole-dipole correlation functions and spectra predicted by our model.

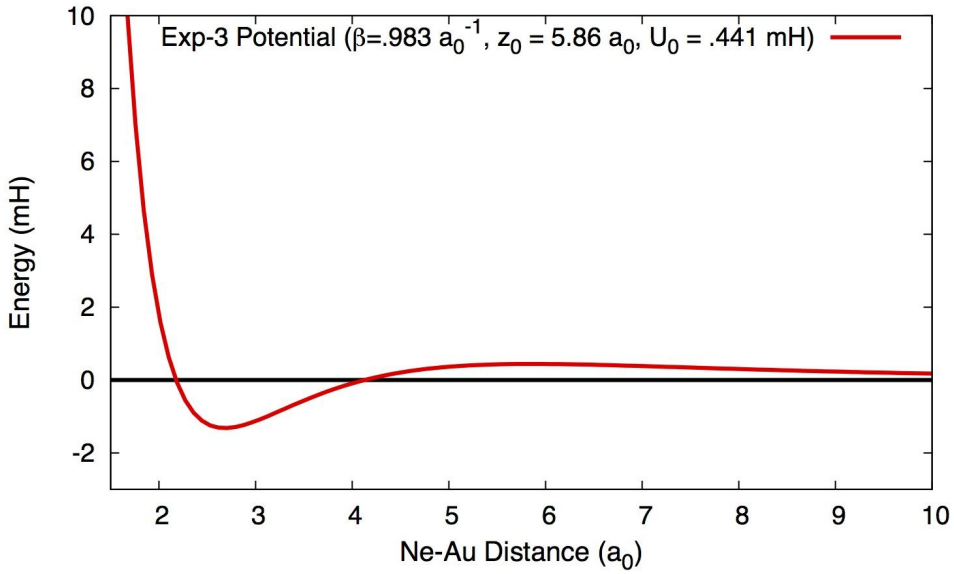

Figure A1:
The adatom-electrode interaction potential for neon on a gold surface as described by an Exp-3 potential.[7] Among the adatoms studied this quarter, neon was one of the most weakly bound to the electrode surface with a well depth of just .441 mHartree.

Figure A2:
The adatom-electrode interaction potential for hydrogen on a gold surface. The long distance H-Au interaction could only be captured by fitting it to an Exp-3 potential supplemented by a number of dispersion terms.

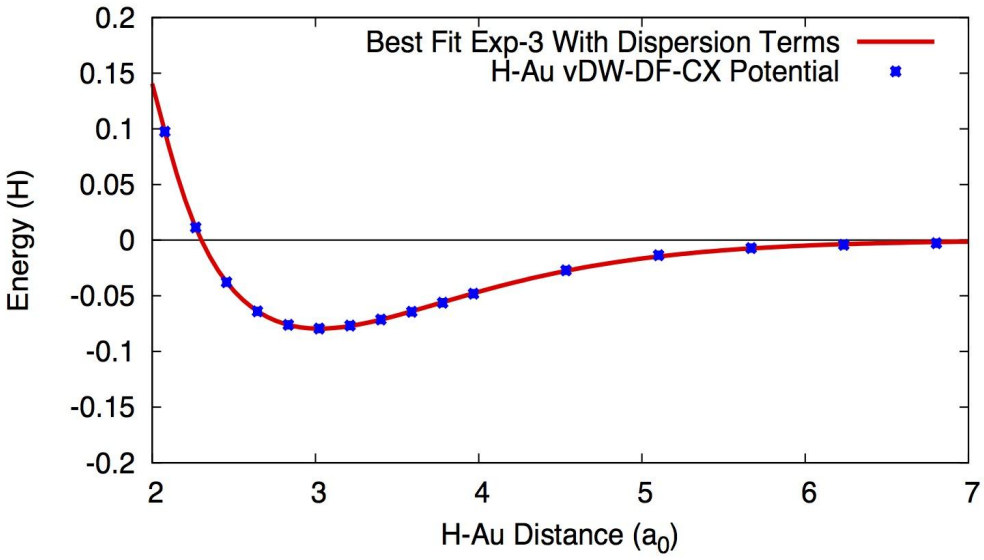

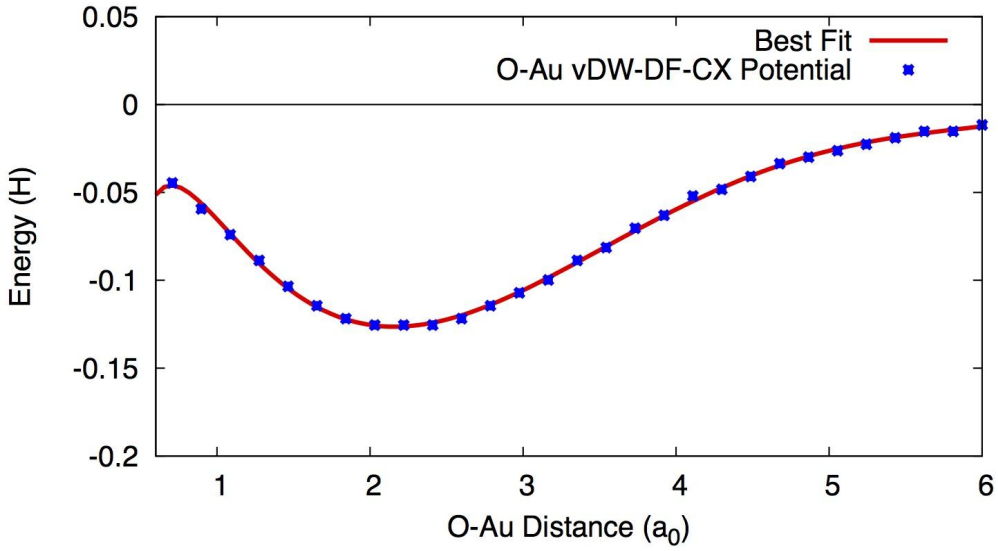

Figure A3:
The adatom-electrode interaction potential for oxygen on a gold surface. Oxygen is tightly bound and its interaction potential exhibits another minimum within the surface.

Figure A4:
The adatom-electrode interaction potential for sulfur on a gold surface. The S-Au interaction is strongly repulsive at small distances.

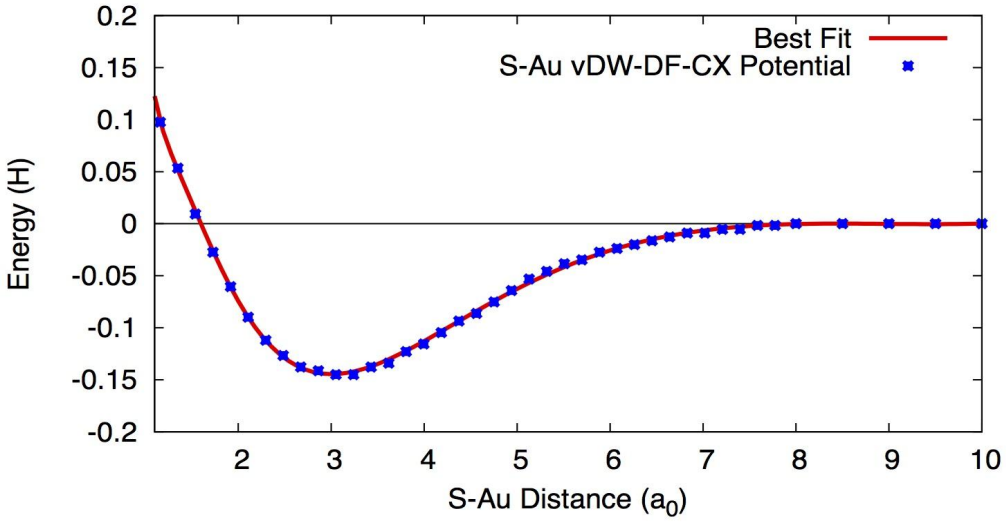

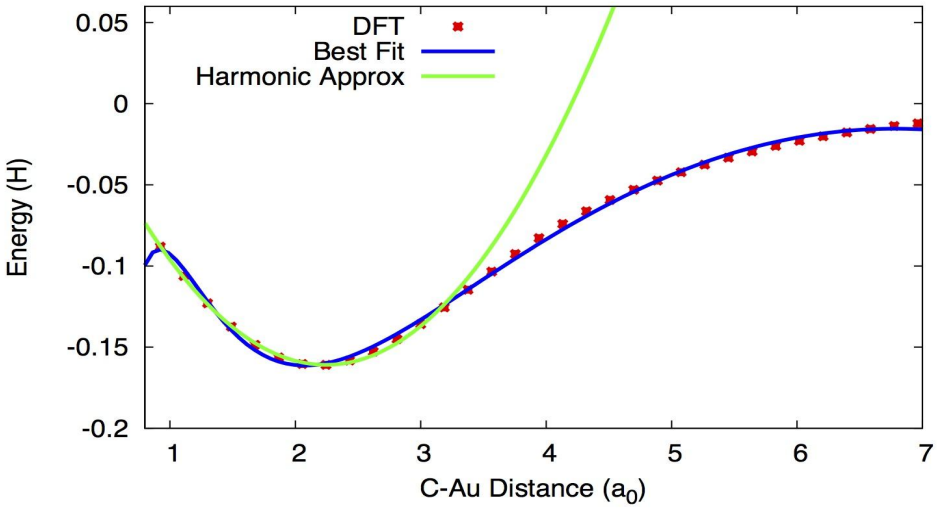

Figure A5:
The adatom-electrode interaction potential for carbon on a gold surface. As with the O-Au potential, the C-Au potential also exhibits a second minimum within the electrode surface.

Figure A6:
The adatom-electrode interaction potential for neon on a silver surface. This interaction potential is similar to those above involving a gold substrate, suggesting that substrates do not alter potentials significantly. Data points were taken from a paper from Ossicini *et al.*[10]

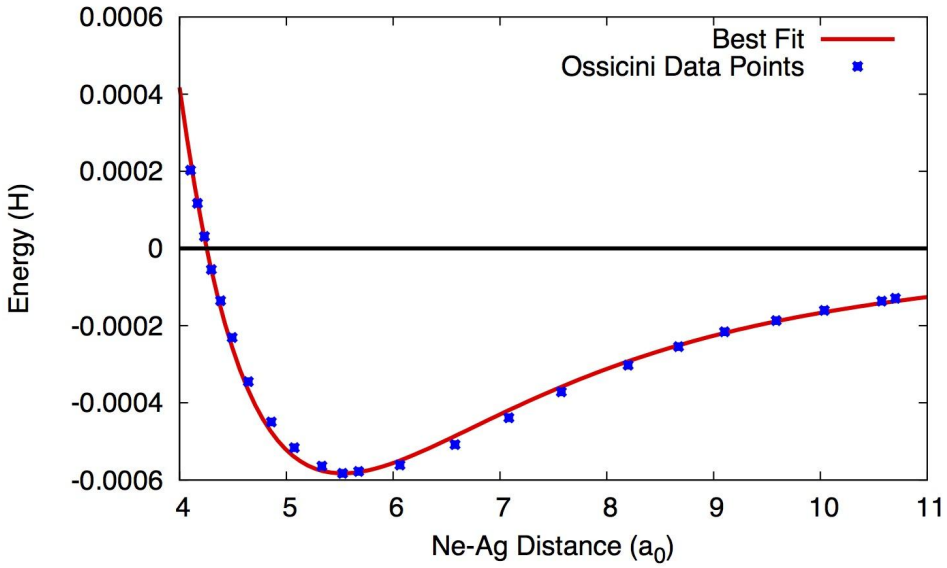

VI. REFERENCES

1. J. Chiaverini and J. M. Sage, *Phys. Rev. A*, **89**, 012318 (2014).
2. C. D. Bruzewicz, J. M. Sage, and J. Chiaverini, *Phys. Rev. A*, **91**, 041402 (2015).
3. D. T. C. Allcock, L. Guidoni, T. P. Harty, C. J. Ballance, M. G. Blain, A. M. Steane, and D. M. Lucas, *New J. Phys.*, **13**, 123023 (2011).
4. K. S. McKay, D. A. Hite, Y. Colombe, R. Jordens, A. C. Wilson, D. H. Slichter, D. T. C. Allcock, D. Leibfried, D. J. Wineland, and D. P. Pappas, arXiv:1406.1778v1 (2014).
5. D. A. Hite, Y. Colombe, A. C. Wilson, K. R. Brown, U. Warring, R. Jordens, J. D. Jost, K. S. McKay, D. P. Pappas, D. Leibfried, and D. J. Wineland, *Phys. Rev. Lett.*, **109**, 103001 (2012).
6. N. Daniilidis, S. Gerber, G. Bolloten, M. Ramm, A. Ransford, E. Ulin-Avila, I. Talukdar, and H. Haffner, *Phys. Rev. B*, **89**, 245435 (2014).
7. A. Safavi-Naini, P. Rabl, P. F. Weck, and H. R. Sadeghpour, *Phys. Rev. A*, **84**, 023412 (2011).
8. Private communication with the Pappas Group (2015).
9. P. R. Antoniewicz, *Phys. Rev. Lett.*, **32**, 1424 (1974).
10. S. Ossicini, *Phys. Rev. B*, **33**, 873 (1986).

Quarterly Report (Sept-Dec, 2015): Epitaxial Aluminum Collaboration

Vincenzo Lordi
Lawrence Livermore National Laboratory
January 15, 2016

Progress During Quarter

During this quarter, we performed a series of STEM simulations on the Al/sapphire interface and also tested the sensitivity of various simulation parameters for producing simulated images best suited for comparison with experiment. The goal is to help understand the structure and composition of experimental epitaxial material grown at LPS and imaged at PNNL. Some insight has resulted in this regard, but work is still ongoing. The basic simulation methodology was reported last quarter.

One of the most important imaging parameters for realistic STEM simulation is the electron beam convergence angle. **Figure 1** illustrates the effect of different convergence angles and also the difference in ideal bright-field (incoherent) STEM imaging and annular dark field imaging. The experimental parameters for the microscope being used at PNNL are 27.5 mrad convergence angle and a HAADF detector with inner and outer angles of 50 and 200 mrad, respectively. The figure illustrates that subtle comparison to experiments requires proper selection of parameters, and also shows the hypothetical improvement in image resolution allowed by a larger convergence angle (effective aperture), for microscopes with exquisitely corrected aberrations. Note that BF simulations do not depend on specimen thickness, but ADF simulations do.

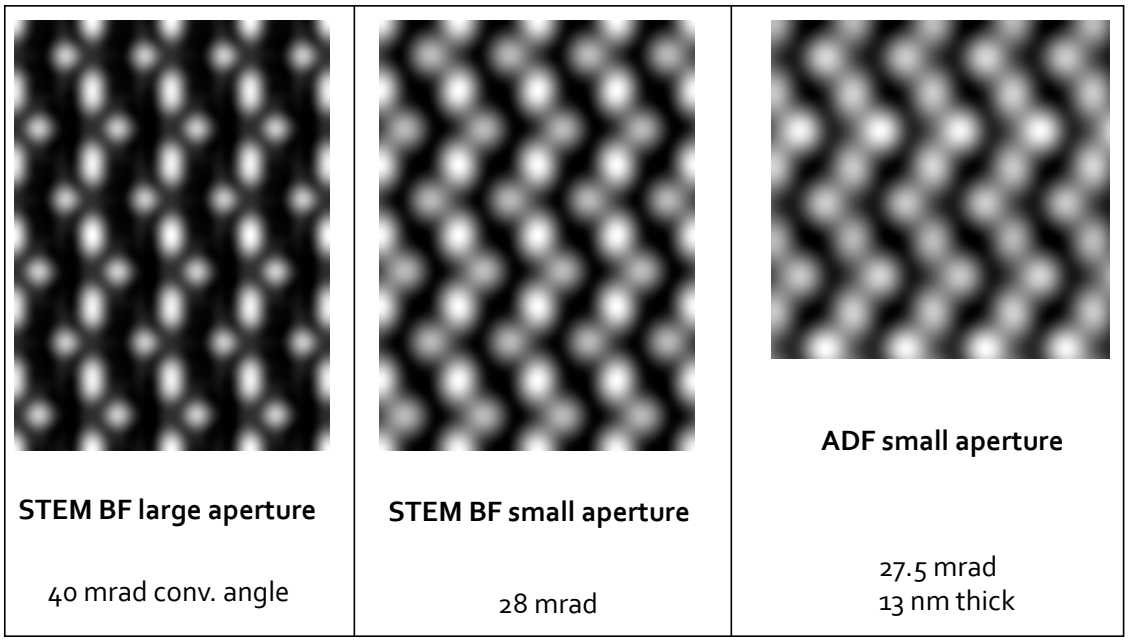

Figure 1. Comparison of convergence angle on the simulated STEM images of crystalline sapphire down the [210] zone axis (left two images, which compare two bright-field STEM simulations), as well as an illustration of the differences between BF and ADF imaging modes (right image).

Figure 2 shows an ADF simulation of a 50 nm thick model of the Al/sapphire interface, based on a DFT-relaxed coherent interface structure (more on this below). This model does not include any dislocations for strain relaxation of the two layers. The model illustrates, however, the qualitative feature of disordered Al columns at the bottom of the nominal bulk Al layer, leading to a reduction in the intensity of those bottom Al spots in the image ("Layer B"). The other major feature is the very dim contrast associated with the upper terminating Al atoms of the sapphire layer ("Layer A_1" and "Layer A_2"), which appear like a streaky extension of the uppermost O columns in the image simulation.

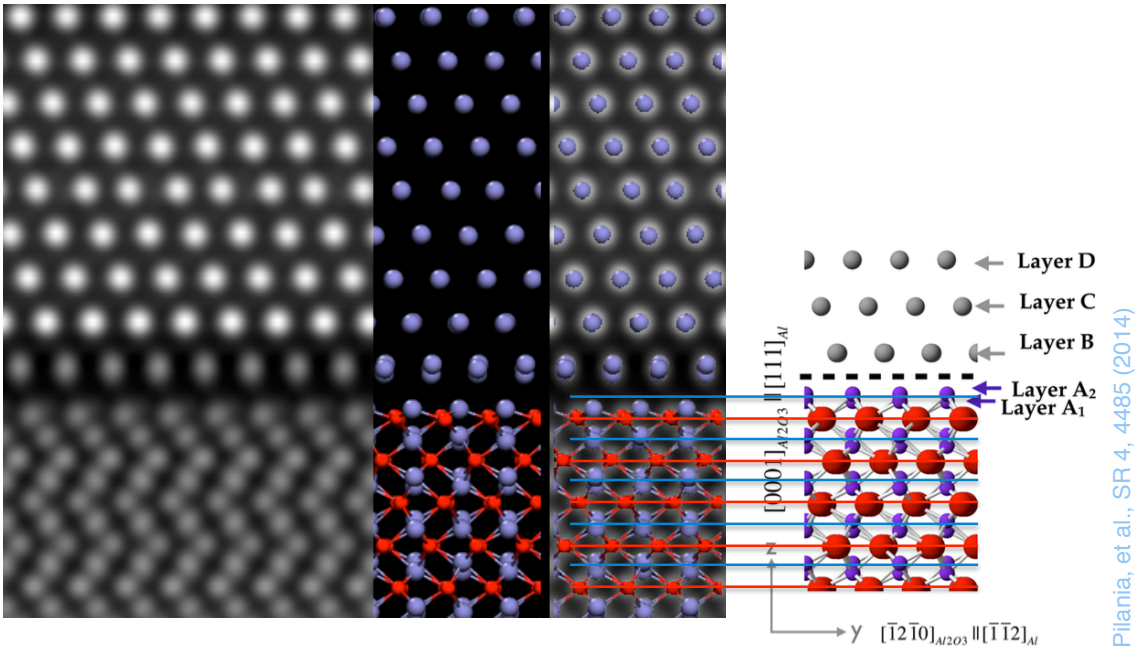

Figure 2. Simulated ADF image of a 50 nm thick perfect, coherently-strained Al/sapphire interface, overlaid with a projection of the atomic model (red = O, purple = Al). A different model obtained with empirical potentials by Pilania, *et al*. is shown to the right for comparison; the details of the atomic column alignment and layer spacing at the interface are the salient differences. ADF simulation of the structure at the right has not been calculated.

To understand possible subtleties of image contrast in experiments and also as a sensitivity study, a series of ADF simulations were performed with different model thicknesses, as shown in **Figure 3**. The simulations demonstrate various contrast patterns associated with very thin samples, for which fewer electron scattering events through the sample lead to noticeably brighter spots for O columns in the sapphire away from the interface, whereas for samples 10's of nm thick this contrast becomes very difficult to distinguish. As a benchmark, **Figure 4** shows a comparison simulated image with no aberrations and also a large convergence angle, to show the image/contrast distortions associated only with the sample thickness (50 nm). This benchmark simulation in some way highlights the ideal, ultimate contrast features in the image.

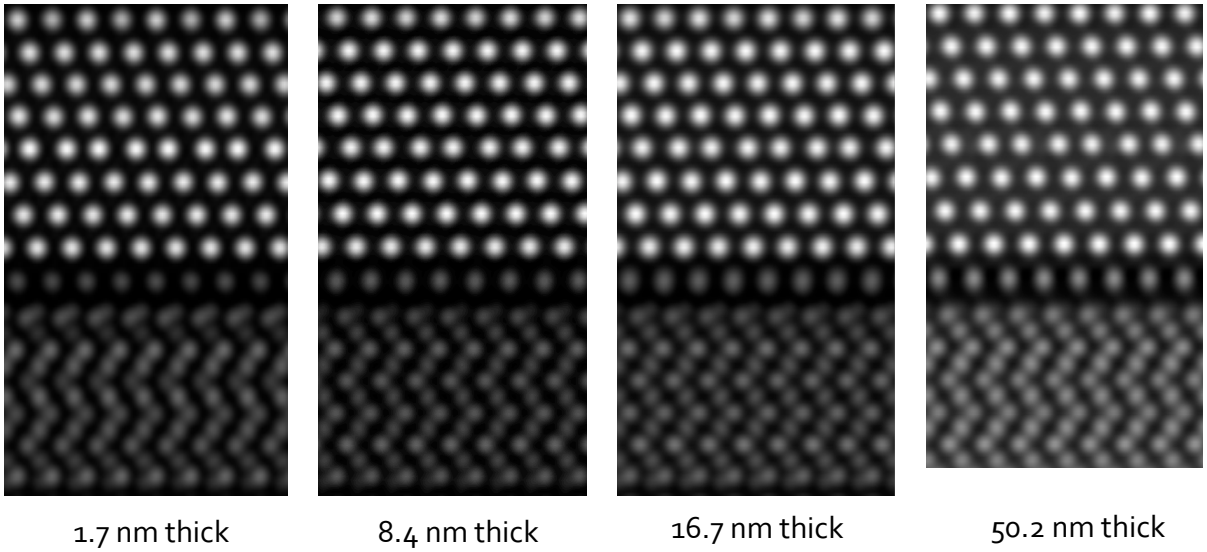

Figure 3. STEM-ADF simulations of the Al/sapphire interface model from Figure 2, with varying model thickness.

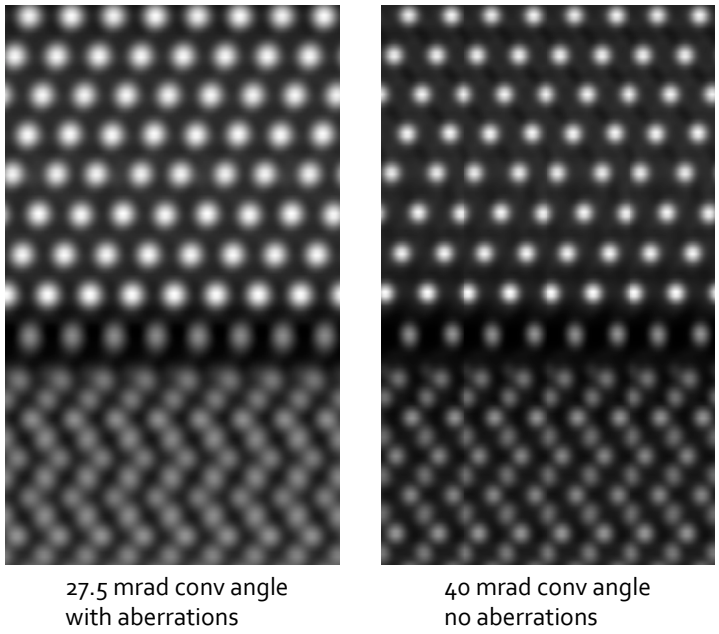

Figure 4. Comparison of STEM-ADF simulations of 50 nm thick Al/sapphire interface model using (left) the full set of microscope parameters including lens aberrations and (right) a larger beam convergence angle and no aberrations. The right image represents a sort of ultimate resolution image.

For comparison with experiment, the model simulations above were overlaid on an experimental image in **Figure 5**. One specific image was chosen for this purpose and is somewhat representative, but does not show all contrast features observed in different experiments. The particular image shown in Figure 5 has a large region with a relaxed coherent interface and apparently (at least) one dislocation. The left smaller image is the original STEM, while the right image shows the same simulation from Figure 2 overlaid three times with different false coloring

and image registry. The leftmost blue overlay was aligned to register with the bulk Al atoms in the top half of the image; the middle red overlay was shifted downward to match the bulk sapphire columns. The mis-registries in the lower and upper layers, respectively, for these two overlays are apparent by the blurriness in the regions so-marked. No scaling was applied to the simulations, so dimensions in the image and simulation are directly comparable. The good matches to the atomic positions in the bulk, combined with the noted mis-registries, indicate that the interface thickness in the model is too small. Indeed, this is demonstrated with the right-most overlay in the image (blue on top and red below), where the simulated image was cut at the interface and separated so that good registry was possible in both of the bulk regions. Incidentally, the upper half of the simulated image also needed to be shifted as indicated, because a dislocation in the vicinity of that region of the image added an extra plane of Al atoms. It is much more apparent in this latter overlay that the interface contrast appears qualitatively captured by the simulation, but that the interface thickness does not quite match.

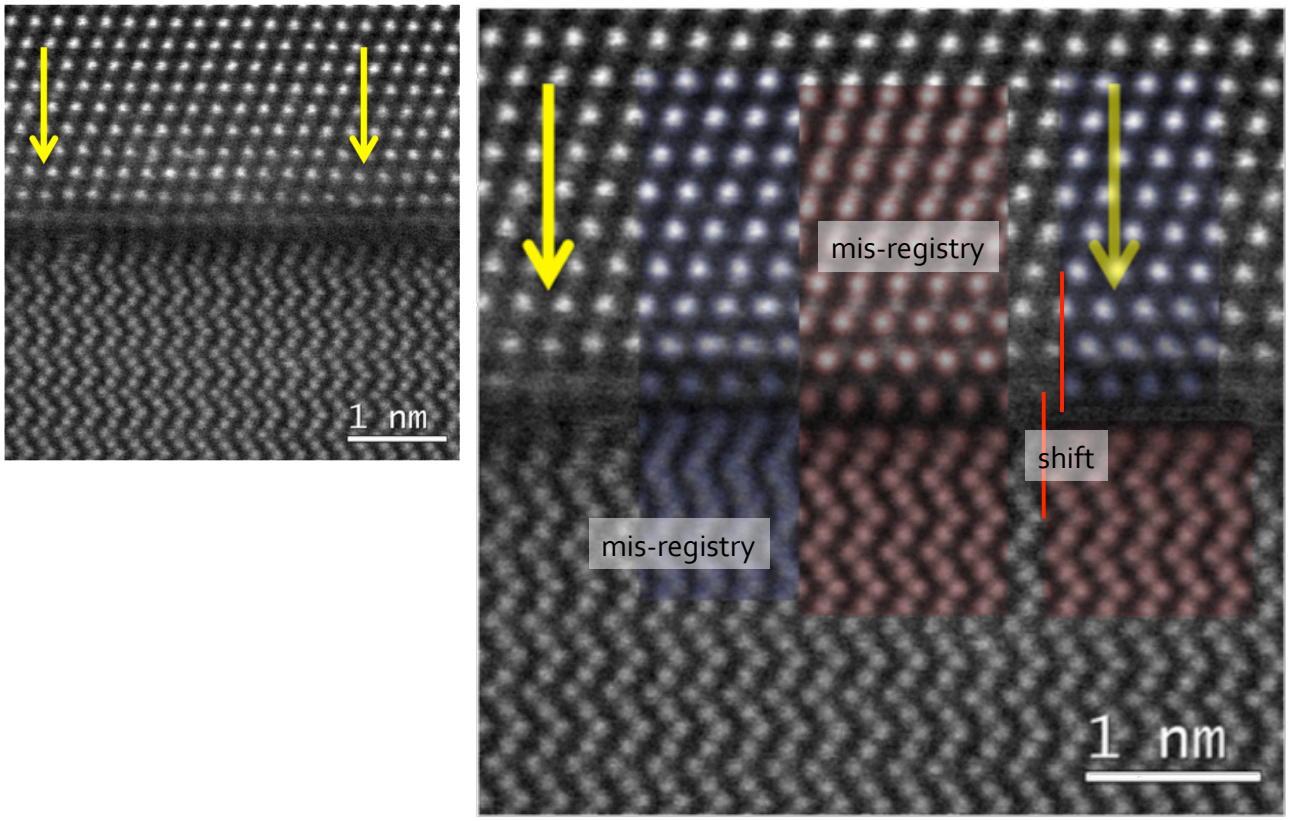

Figure 5. Image overlay between simulated and experimental STEM-ADF images of the Al/sapphire interface. See the text above for a description of the annotations on the image. The smaller image on the left is the original experimental image, while the right side of the figure shows the simulated images overlaid in semi-transparent false color (blue and red).

Since the bulk portions of the Al/sapphire interface model described above fit the experiments well, but the interface width is too small, we investigated the effects of different interface relaxations on the simulated structure and corresponding STEM-ADF images. The strained coherent interface structure above has constrained cell dimensions to force a coherent

interface, based on slices and empirical molecular dynamics simulations (Streitz-Mintmire potential) used to generate the interface. Two structures with different interface relaxations were generated for comparison, based on extreme cases for the interface relaxation, and are shown in **Figure 6**. The most extreme case is a full relaxation of all cell dimensions and atomic coordinates, which physically would correspond to a thin coherent bi-layer, shown in the middle panel of Figure 6. A slight widening of the interface is observed, along with a distinct separation of the first bulk Al layer, which manifests as elongated spots in the simulated STEM image. This model clearly does not reproduce the experimental contrast, but demonstrates that a larger interface separation is reasonable. The right panel of Figure 6 shows a hypothetical fully-coherently-strained epitaxial Al film on a bulk sapphire substrate, generated by allowing only the vertical lattice dimensions of the Al to relax; while this is a more reasonable model, it overestimates the Poisson expansion in the vertical direction (of the interface and the bulk Al), because the strain relaxation from misfit dislocations observed experimentally is not accounted. Nonetheless, the expanded interface width is again demonstrated and may be more realistic than the "original" model above and in the left panel of Figure 6. The more complicated contrast associated with the split layer of Al at the interface, along with the reduced brightness associated with disorder (in the lower Al layer of the Z-relax model or in the interface Al layer of original model), may indicate the kind of contrast seen in experiments.

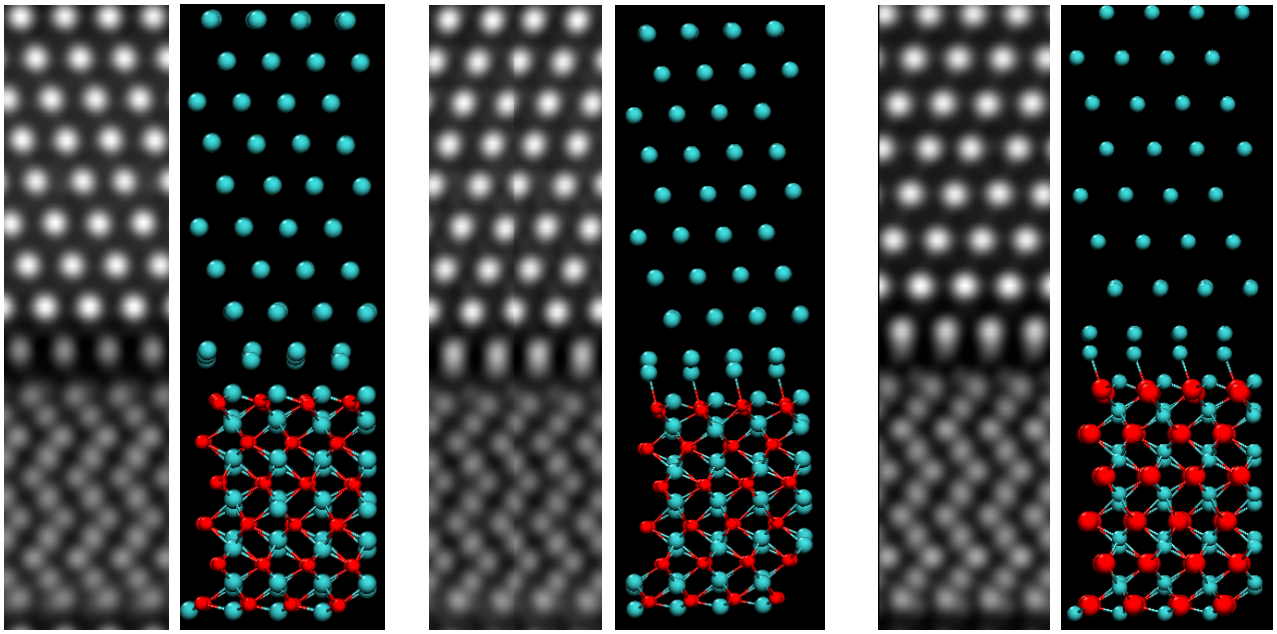

Figure 6. STEM-ADF simulations and associated models for different interface structures generated by DFT relaxations. The left model corresponds to the structure shown in Figures 2-5 and simulates a coherently strained interface without any Poisson relaxation in the vertical (*Z*) direction. The middle model is fully relaxed in atomic coordinates, cell shape, and cell volume; this extreme model would represent the situation for two nm-scale-thick films of Al and sapphire coherently attached with no misfit dislocations. The right model represents an epitaxial Al film grown strained on a single-crystal sapphire substrate; the sapphire in-plane lattice constant is preserved, but vertical relaxation of the interface is allowed. Increases in the interface thickness is observed for the relaxed models, as well as changes in the contrast of interface models All models are 50 nm thick. (red = O, cyan = Al)

A reasonable model for the observed contrast features in STEM-ADF images of the Al/sapphire interface away from misfit dislocations has been presented, which is based on a coherent interface. Reduced contrast at the interface associated with interface expansion and disorder of the Al columns was shown by simulations, in agreement with many experimental observations, demonstrating that impurities or vacancies are not required for such contrast. However, the models do not explain the whole of experimental observations, which show various features in different samples and sample regions; in addition, interface steps are observed which we have not attempted to simulate. The general model framework presented here, along with the image simulation methodology, represents a reliable baseline for studying more complicated interface compositions and structures for comparison with experiment.

Future Work

Activities in the up-coming quarter will focus on extending the STEM-ADF simulations to help understand misfit dislocation structures observed experimentally. For this task, we will rely partly on large models of such misfit dislocation networks generated using empirical potentials by the group at Los Alamos National Lab (Ben Liu, Steve Valone, *et al.*). We will simulate STEM-ADF images from the dislocation model at various thicknesses. In addition, smaller pieces of the dislocation model will be extracted and relaxed with DFT to study the differences in structure predicted by the two methods. Interface models containing point defects may also be studied.

In addition, analogous work on the Al/Si interface will be pursued.

Longer term, electronic structure calculations of the misfit dislocation structures are planned, to study possible mechanisms for introducing noise into quantum devices fabricated with such interfaces.